minerals

MDPI

Article

Potassic-Hastingsite from the Kedrovy District (East Siberia, Russia): Petrographic Description, Crystal Chemistry, Spectroscopy, and Thermal Behavior

Ekaterina Kaneva [1,2,*], Tatiana Radomskaya [1,2], Roman Shendrik [1], Victor Chubarov [1] and Victoria Danilovsky [3]

[1] Vinogradov Institute of Geochemistry, Siberian Branch of the Russian Academy of Sciences, 664033 Irkutsk, Russia; taniaojigova@mail.ru (T.R.); r.shendrik@gmail.com (R.S.); chubarov@igc.irk.ru (V.C.)
[2] Department of Subsoil Use, Irkutsk National Research Technical University, 664074 Irkutsk, Russia
[3] Sobolev Institute of Geology and Mineralogy, Siberian Branch of the Russian Academy of Sciences, 630090 Novosibirsk, Russia; victoria.saratovkina@gmail.com
* Correspondence: kev604@mail.ru

Abstract: In this work we report on a petrographic, crystal-chemical, and optical characterization, obtained from different analytical methods, of amphibole species. Potassic-hastingsite, ideally $^{A}K^{B}Ca_2{}^{C}(Fe^{2+}{}_4Fe^{3+})^{T}(Si_6Al_2)O_{22}{}^{W}(OH)_2$, has been found in the Kedrovy district (East Siberia, Russia). The sample occurs as well-formed and large radially radiant aggregates of dark green, almost black crystals. The unit cell dimensions are a = 9.9724(3) Å, b = 18.2968(4) Å, c = 5.3573(1) Å, β = 104.945(3)°, V = 944.44(4) Å^3, Z = 2. Site populations were determined by combining single-crystal structure refinement and electron probe microanalysis, and Fe^{3+}/Fe^{2+} ratio was obtained from X-ray fluorescence analysis. Infrared, diffuse light UV/Vis/NIR absorption, and electron spin resonance spectra are presented and discussed. A thermoelastic behavior of a powder of potassic-hastingsite was studied by in situ high-temperature X-ray diffraction. A thermal expansion and subsequent significant contraction in the unit cell volume during a high-temperature X-ray powder diffraction experiment is observed as a consequence of the deprotonation process, which is locally balanced via oxidation of Fe^{2+}. According to the data obtained for potassic-hastingsite, these processes occur within 400–600 °C. The thermal expansion of the mineral is anisotropic; the thermal expansivity coefficients α_a:α_b:α_c ($\times 10^{-6}$) = −18.06:9.59:−1.09 at 400 °C, −26.15:−1.52:2.22 at 600 °C and 23.77:−25.06:42.08 at 750 °C.

Keywords: potassic-hastingsite; amphiboles; petrography; mineral associations; crystal chemistry; IR spectroscopy; electron spin resonance; absorption spectroscopy; thermal behavior

Citation: Kaneva, E.; Radomskaya, T.; Shendrik, R.; Chubarov, V.; Danilovsky, V. Potassic-Hastingsite from the Kedrovy District (East Siberia, Russia): Petrographic Description, Crystal Chemistry, Spectroscopy, and Thermal Behavior. *Minerals* **2021**, *11*, 1049. https://doi.org/10.3390/min11101049

Academic Editors: Gioacchino Tempesta and Giovanna Agrosì

Received: 21 August 2021
Accepted: 24 September 2021
Published: 27 September 2021

1. Introduction

Hastingsite is an end-member of the calcium amphiboles subgroup [1], which form translucent to opaque platy or grainy, acicular, radiating, fibrous, columnar crystals having a black, dark-green, greenish-brown, tan, or brown to yellow color. Hastingsite was discovered and named in 1896 by F. D. Adams and B. J. Harrington for the type locality in Hastings County (Canada).

According to the nomenclature of the amphibole-supergroup [2,3] the general formula of the amphiboles is $AB_2C_5T_8O_{22}W_2$, where A = □, Na, K, Ca, Pb, Li; B = Na, Ca, Mn^{2+}, Fe^{2+}, Mg, Li; C = Mg, Fe^{2+}, Mn^{2+}, Al, Fe^{3+}, Mn^{3+}, Ti^{4+}, Li; T = Si, Al, Ti^{4+}, Be; W = (OH), F, Cl, O^{2-}.

Hastingsite has the ideal formula $NaCa_2(Fe^{2+}{}_4Fe^{3+})(Si_6Al_2)O_{22}(OH)_2$. The observed variations in the end-member formula recognized by the IMA for hastingsite are reported in Table 1. Detailed crystal-chemical properties of the minerals have been investigated, sometimes using a multi-technique approach consisting of electron probe microanalysis, Mössbauer spectroscopy, and single-crystal X-ray refinements [4–21]. However, rela-

tively few studies on their structural behavior under non-ambient conditions have been made [22,23].

Table 1. Previously published selected data on hastingsites.

Name (Year of Naming)	Chemical Formula	Type Locality	Ref.	Abbr.
Hastingsite (1896)	$NaCa_2(Fe^{2+}{}_4Fe^{3+})(Si_6Al_2)O_{22}(OH)_2$	Dungannon Township, Hastings County, Ontario, Canada.	[4–6]	Hs
Potassic-hastingsite (2020)	$KCa_2(Fe^{2+}{}_4Fe^{3+})(Si_6Al_2)O_{22}(OH)_2$	Keshiketeng Banner, Inner Mongolia, China	[7–10]	K-Hs
Potassic-fluoro-hastingsite (2009)	$KCa_2(Fe^{2+}{}_4Fe^{3+})(Si_6Al_2)O_{22}F_2$	Greenwood mine, Town of Tuxedo, New York, USA	[11]	K-F-Hs
Potassic-chloro-hastingsite (2005)	$KCa_2(Fe^{2+}{}_4Fe^{3+})(Si_6Al_2)O_{22}Cl_2$	Dashkesan Co-Fe deposit, Dashkesan district, Azerbaijan	[12,13]	K-Cl-Hs
Magnesio-hastingsite (1928)	$NaCa_2(Mg_4Fe^{3+})(Si_6Al_2)O_{22}(OH)_2$	Mont Royal, Monreal, Quebec, Canada	[14–16]	Mg-Hs
Potassic-magnesio-hastingsite (2006)	$KCa_2(Mg_4Fe^{3+})(Si_6Al_2)O_{22}(OH)_2$	Ylmenogorsky complex, South Urals, Russia	[17,18]	K-Mg-Hs
Magnesio-fluoro-hastingsite (2006)	$NaCa_2(Mg_4Fe^{3+})(Si_6Al_2)O_{22}F_2$	Uroi Hill, Simeria, Hunedoara, Romania	[19,20]	Mg-F-Hs
Oxo-magnesio-hastingsite (2013)	$NaCa_2(Mg_2Fe^{3+}{}_3)(Si_6Al_2)O_{22}O_2$	Deeti volcanic cone, Gregory rif, northern Tanzania	[21]	O-Mg-Hs

This work is devoted to the description of a new occurrence of potassic-hastingsite found in the Kedrovy district (East Siberia, Russia). Despite the fact that the mineral and the name were approved by IMA–CNMMN in 2018, and the description of the holotype was published in 2020 [10], this species of hastingsite was widely known and reported in early works. High-potassium hastingsites from Yukon (Canada) [7], West Ongul Island (East Antarctica) [8], and Vlastějovice (Czech Republic) [9] were described before approval.

In this paper we report the results of the petrographic study, crystal-chemical characterization, and thermal behavior investigation of potassic-hastingsite. Attention is focused on the thermal expansion and structural evolution with temperature. Additional infrared spectroscopy, diffuse-light absorption spectroscopy in the ultraviolet (UV), visible (Vis) and near infrared (NIR) spectral region, and electron spin resonance studies were carried out for a more detailed characterization of the optical properties of the studied potassic-hastingsite and the processes occurring during its heating.

2. Materials and Methods

2.1. Sample Description

A skarn sample containing potassic-hastingsite used for this study is derived from the collection of the Sidorov Mineralogical museum of INRTU (Irkutsk, Russia). The specimen was found in the Kedrovy district, located 10 km northeast of the urban Vitimskoye settlement upstream of the Malaya Severnaya River (Mamsko-Chuisky area, Irkutsk Region, East Siberia, Russia) (Figure 1). The skarn sample was taken in the zone of contact-metasomatic impact of Paleozoic granitoids (Konkudero-Mamakan and Mamsk complexes) on the host strata (marbleized limestones and shales of the Sogdiondonskay Formation (PR_3sg)).

The morphogenetic features of potassic-hastingsite and its paragenetic relationship with associated minerals were studied by optical petrographic methods using an Olympus BX-51 polarizing microscope (Olympus Co., Tokyo, Japan) in transmitted light.

The sample is a rock fragment (7 cm × 4 cm × 3 cm), composed mainly of intergrowths and radial-radiant aggregates of dark green, almost black potassic-hastingsite, brown-orange garnet, purple vesuvianite, and small amounts of calcite, quartz, and sulfides

(Figure 2). Apatite and zircon were identified as accessory minerals. Zoisite and epidote are found as single grains. Minerals are unevenly distributed. The structure is coarse-grained.

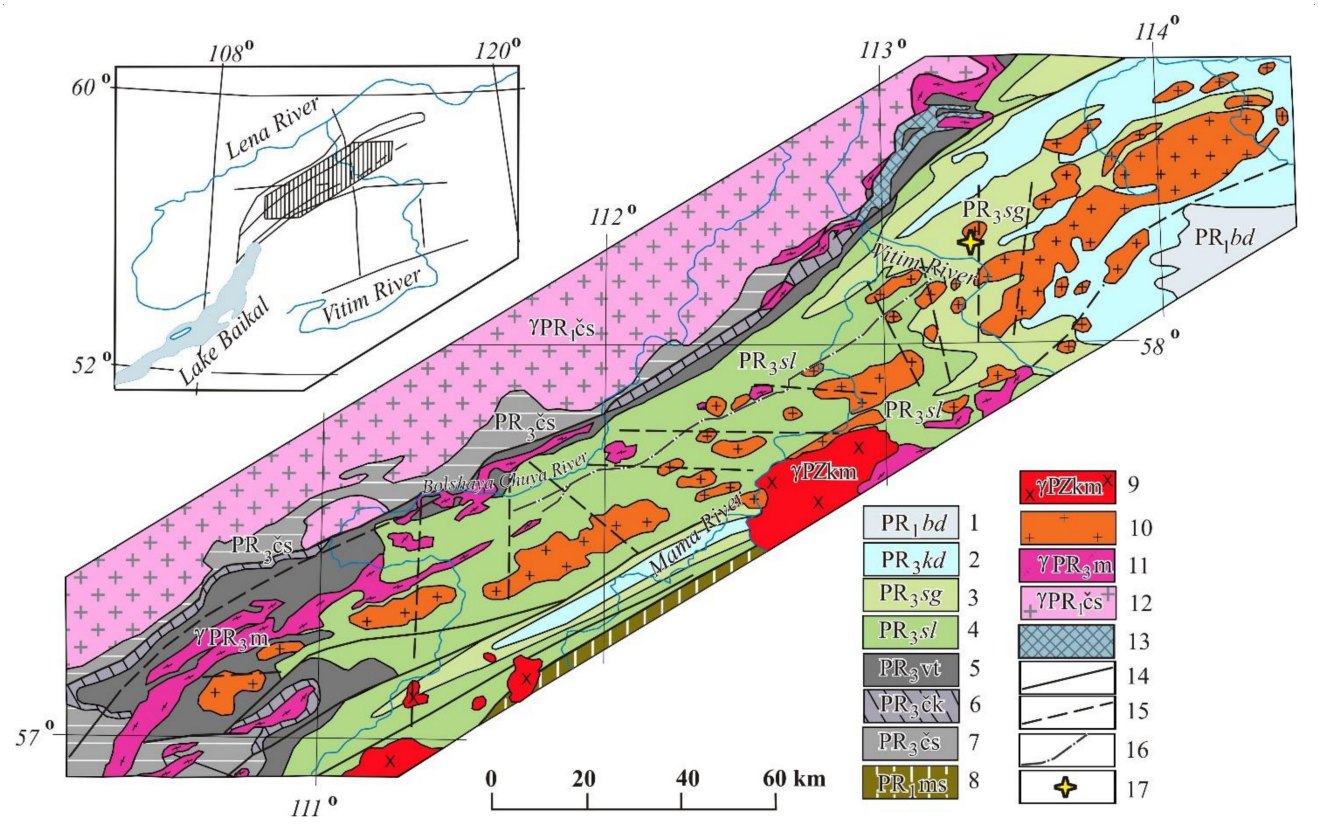

Figure 1. Geological map of the Mamsksk mica-bearing province modified after [24]. 1—Bodaibo subseries: Vachskaya, Anangrskaya, Dogaldynskaya and Iligirskaya combined formations—carbonaceous quartzites, carbonaceous shales, sandstones and siltstones, phyllitic shales; 2—Kadalikanskaya subseries: Konkuderskaya, Shusmanskaya, Khomolkhinskaya, Imnyakhskaya, Bodaibokanskaya combined formations—scapolite-biotite and biotite spotted shales and crystalline limestones, marbles, in zones of low-grade metamorphism—sericite-quartz "carbonaceous" limestones; 3–6— Mamskaya subseries: 3—Sogdondonskaya suite, 4—Slyudyankinskaya suite, 5—Vitimskaya suite, 6—Chukchinskaya and Yakdakarskaya combined formations—metagravelites and metaarkosic sandstones, quartzites, amphibolites and amphibole gneisses, disten-garnet-staurolite and two-mica schists; 7—Chuyskaya and Ukuchiktinskaya strata – migmatites and granite-gneisses, biotite, hornblende-biotite and pyroxene gneisses, sillimanite schists; 8—Muyskaya strata—sandstones, siltstones, chlorite-biotite, quartz-sericite and biotite schists, quartzites, orthoschists; 9—Konkudero-Mamakan complex–amphibole-biotite and biotite granites, granodiorites and granosyenites; 10–11—Mamsko-Oron complex: 10—Second phase: granite-pegmatites, K-feldspar pegmatites, mica-bearing pegmatites; 11—first phase: amphibole-biotite and biotite gneiss-granites, plagiogranites, basic plagioclase pegmatites; 12—Chuya-Kodar complex—porphyritic and uniformly granular hornblende-biotite and biotite granites, leucocratic granites, plagiogranites, pegmatites; 13—orthoamphibolites; 14—tectonic faults tracked and confirmed by geophysical data; 15—alleged tectonic faults based on geophysical data, 16—thrust zones filled with tectonites, migmatized gneisses with magnetite; 17—sampling point.

In the thin section, euhedral and subhedral elongated prismatic crystals of amphibole (10 mm × 2.5 mm × 1.5 mm) exhibit pleochroism, which is characteristic of the hastingsites: light brownish green on Np, dark olive-green on Nm, blue-green on Ng (Figure 3a,b). Potassic-hastingsite crystals are anhedral relatively to euhedral garnet crystals (Figure 3c,d). Amphibole contains inclusions of colorless euhedral prismatic elongated crystals of apatite (up to 0.5 mm × 0.3 mm in size) (Figure 3e,f) and zircon grains (up to 0.2 mm × 0.1 mm in size). Around zircon enclosed in amphibole, pleochroic haloes are formed. Zircon is most likely a relict mineral. Sulfides (pyrite) and the products of their oxidation (minerals of the limonite group) (Figure 3g,h) are found along cleavage and cataclase cracks in potassic-hastingsite.

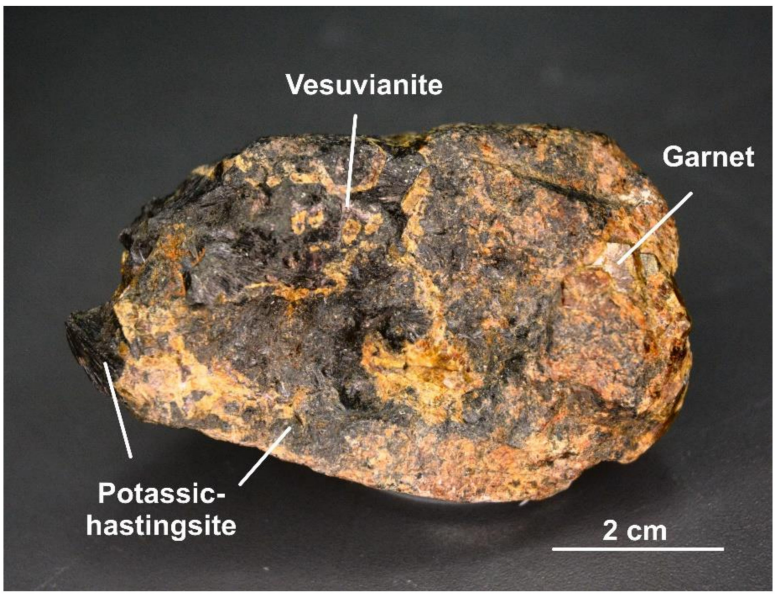

Figure 2. Skarn sample.

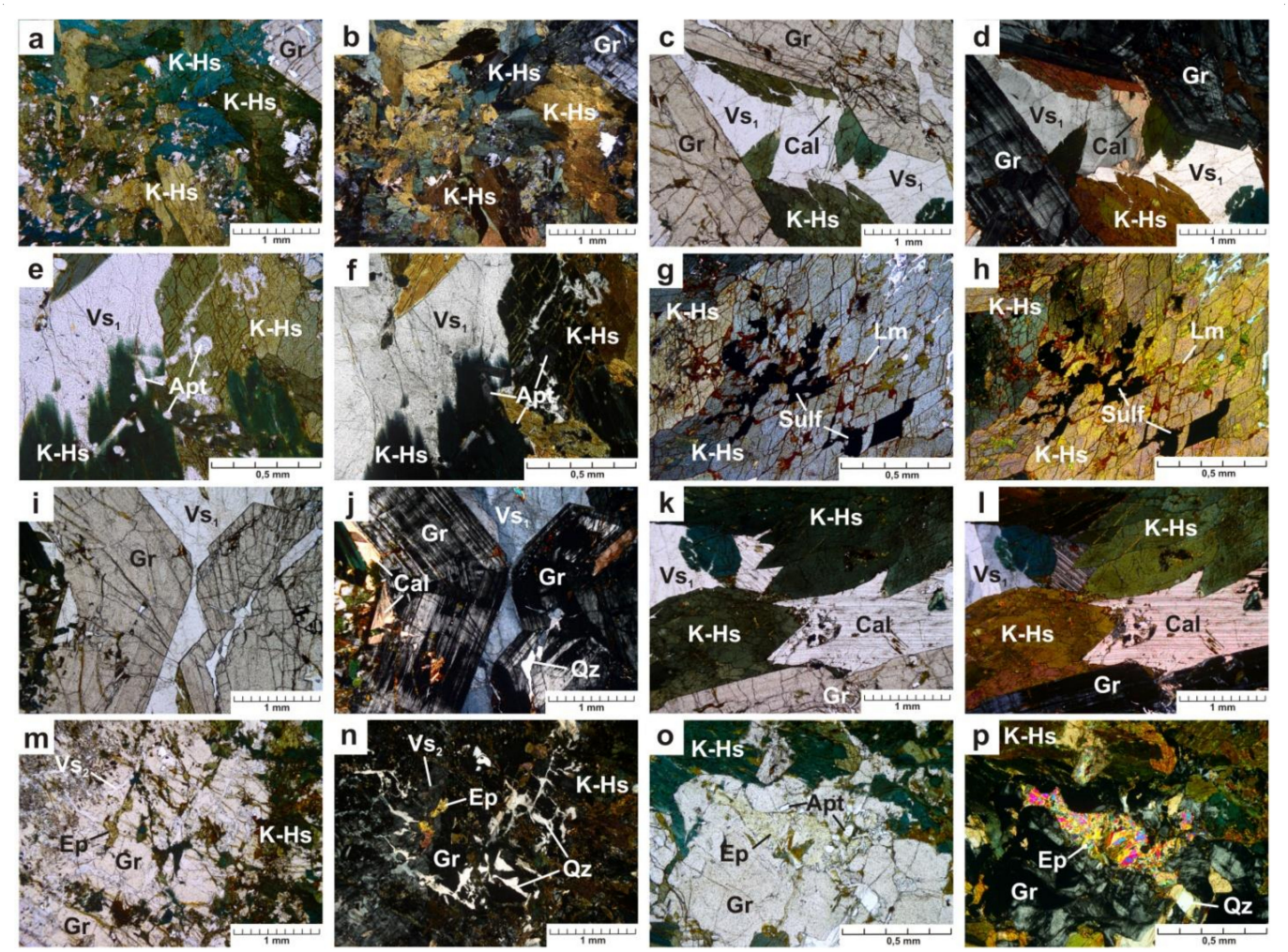

Figure 3. Photomicrographs of the mineral assemblages and their textural properties in a thin section in transmitted light, (**a**,**c**,**e**,**g**,**i**,**k**,**m**,**o**)—plane polarised light and (**b**,**d**,**f**,**h**,**j**,**l**,**n**,**p**)—cross polarised light image. Cal—calcite, Ep—epidote, Gr—garnet, K-Hs—potassic-hastingsite, Lm—minerals of the limonite group, Qz—quartz, Sulf—sulfides, Vs_1 and Vs_2—vesuvianite of the first and second generation, respectively. Mineral abbreviations are used according to [3,25].

Garnet crystals in the thin section are skeletal formations up to 1 cm in size with a faint yellow tint. The central parts of them are filled with intergrowths of garnet, potassic-hastingsite, and vesuvianite, while the peripheral part is composed only of garnet (Figure 3i,j). Moreover, the edges are euhedral. Through crossed polarizers, the mineral exhibits anomalous interference coloration: alternating isotropic and anisotropic zones (Figure 3j). Such zoning is typical for grossular-andradite garnets [26–28]. Garnet grains are broken by numerous cataclase cracks filled with vesuvianite, quartz, and sulfides.

Colorless subhedral crystals of calcite (up to 2 mm) are irregularly distributed and anhedral relative to potassic-hastingsite and garnet (Figure 3c,d,k,l).

Vesuvianite is found in two generations. The first one is associated with potassic-hastingsite, garnet, and calcite, in relation to which the mineral is anhedral (Figure 3c–f,i–l). The grain size varies from 1 to 4 mm. Vesuvianite of the second generation fills the cracks of cataclase (Figure 3m,n). Its grains exhibit weak pleochroism, from light lilac to light yellow, and anomalous interference coloration of brownish lilac and gray.

Quartz fills the cracks of cataclase, and has a superimposed nature of formation (Figure 3m–p). Large sulfide grains (up to 1 mm) are euhedral and subhedral. They have a characteristic rim of iron hydroxides. Sulfides were also found filling cleavage and catclase cracks.

In thin sections, single grains of epidote and zoisite can be noted (Figure 3m–p).

2.2. Chemical Analysis

Mineral chemistry was analyzed in ~0.2–0.6 mm grains on a JEOL JXA-8230 electron probe microanalyzer (Jeol, Tokyo, Japan). The electron probe microanalyses (EPMA) were performed with a 20 kV accelerating voltage, 10 nA beam current, and a ~10 μm spot size in wavelength-dispersive spectroscopic (WDS) mode. The composition was determined with reference to the following standards: F—phlogopite (Si, Al, K, Mg, F), diopside (Ca), albite (Na), Mn-garnet rhodonite (Mn), pyrope (Fe), Ti—glass (Ti), Cl—apatite (Cl), and Cr—pyrope (Cr). A conversion from X-ray counts to oxide weight percentages (wt%) was obtained with the ZAF matrix correction [29]. Chemical composition results, obtained from 16 analyses, show that the samples examined are relatively homogeneous: Al_2O_3 (10.4–11.2 wt%), SiO_2 (36.2–37.1 wt%), Na_2O (0.8–1.2 wt%), CaO (10.9–11.2 wt%), K_2O (2.0–2.3 wt%), FeO (33.2–34.3 wt%), MgO (0.8–1.2 wt%), MnO (0.34–0.40 wt%), TiO_2 (0.20–0.24 wt%), Cl (1.8–2.3 wt%), and F (0.11–0.20 wt%) contents (97.9–98.4 wt% total). OH-group content was calculated from the charge balance.

Determination of Fe^{2+} and Fe^{3+} was performed using the X-ray fluorescence (XRF) technique based on the measurement of the relative intensity of the X-ray emission line influenced by the iron chemical state ($FeK\beta_5$). This technique was developed for rocks analysis [30–32] and successfully applied for iron valence state assessment in picroilmenites [33]. Calibration curves were constructed using certified reference materials of igneous rock of ultrabasic composition with certified values of total and ferrous iron, iron minerals (hematite, magnetite), and amphibole samples analyzed by certified volumetric and atomic absorption techniques. Samples were prepared as pressed pellets on a boric acid substrate. Measurements were performed on a wavelength-dispersive X-ray fluorescence spectrometer S4 Pioneer (Bruker AXS, Berlin, Germany).

2.3. Structural Analysis

Single crystal X-ray diffraction analysis (SCXRD) of the selected single crystal was carried out by means of a Bruker AXS D8 VENTURE automated diffractometer (Bruker AXS, Berlin, Germany) with graphite-monochromatized Mo*Kα* radiation at room temperature. Operating conditions were: 50 kV and 1 mA, with a crystal-to-detector distance of 40 mm. A set of 24 frames was used for initial cell determination with a strategy optimized by the APEX2 suite package [34]. Data collection was accomplished by several φ and ω scans with 0.3° rotation and 4.3 s exposure time per frame. The half of the Ewald sphere ($\pm h$, $\pm k$, $\pm l$) was recorded up to θ_{max} ~ 40°. 40,291 reflections were measured, of which 2568

were independent. Data reduction was performed using CrysAlisPro Version 1.171.39.46 (Rigaku, Tokyo, Japan) [35]. Anisotropic structure refinement was carried out using the program CRYSTALS [36] in the space group *C*2/*m*. The refined parameters were: scale factor, atom positions, anisotropic displacement parameters. In the refinement, the site population and nomenclature defined by [37,38] were used. Unit cell parameters, some details on data collection, and summary results from structure refinements are reported in Table 2.

Table 2. Selected data on single crystal, data collection, and structure refinement parameters of the studied potassic-hastingsite sample.

Crystal Data		**Data Collection**	
Crystal system	Monoclinic	Theta range	2.226° to 38.221°
Space group	*C*2/*m*	Reflection measured	40,291
Temperature (K)	293	Independent reflections	2568
a (Å)	9.9724(3)	$R_{merging}$ [$R_{(int)}$] (%)	3.70
b (Å)	18.2968(4)	h_{min}, h_{max}	−17, 17
c (Å)	5.3573(1)	k_{min}, k_{max}	−31, 31
β (°)	104.945(3)	l_{min}, l_{max}	−9, 9
V (Å^3)	944.44(4)	**Refinement**	
Z	2	Reflections used in the refinement (I > 3$\sigma_{(I)}$)	1851
Radiation type	X-ray, λ = 0.7107 Å	N. of refined parameters	124
Crystal shape	tabular	*R* [a] [on *F*] (%)	2.71
Crystal dimensions (mm)	0.14 × 0.10 × 0.08	R_w [b] [on *F*] (%)	2.92
Crystal color	brownish-black	Goof [c]	1.0726
Calculated density (g/cm^3)	3.485	$\Delta\rho_{min}/\Delta\rho_{max}$ (e$^-$/Å^3)	−0.79/0.88

[a] $R = \Sigma[|F_o| - |F_c|]/\Sigma|F_o|$. [b] $R_w = [\Sigma[w(F_o^2 - F_c^2)^2]/\Sigma[w(F_o^2)^2]]^{1/2}$; *w* = Chebyshev optimized weights. [c] Goodness-of-fit = $[\Sigma[w(F_o^2 - F_c^2)^2]/(N - p)]^{1/2}$, where N and p are the number of reflections and parameters, respectively. *F*—structure factor.

The CIF was deposited with the Cambridge Crystallographic Data Centre (CSD 2102019).

A figure showing structural details was prepared using the program VESTA (version 4.3.0, Tsukuba, Japan) [39].

High-temperature X-ray powder diffraction (HTXRPD) data of the studied sample were collected in air with a Bruker D8 ADVANCE powder diffractometer (Bruker AXS, Berlin, Germany) with Bragg-Brentano geometry (Cu-Kα radiation, 40 kV, 40 Ma). The XRPD system is equipped with a HTK16 heating chamber. The powder was deposited on a PtRh substrate, assuring a direct homogeneous heating and fast temperature ramping. The sample was found to be single phase.

Profiles were obtained between 7° and 65° 2θ with a step size of 2θ—0.02° and a counting time of 1 s per step. The temperature step of the heating and cooling rate was 25 °C/min stepwise at discrete steps of 50 °C up to 750 °C and of 100 °C down to 30 °C with an equilibration time of 2 min.

The structural model of potassic-hastingsite obtained by SCXRD was taken as a starting for the refinement of the unit cell parameters performed using TOPAS 4.2 software package (Bruker AXS, Berlin, Germany) [40]. The background was modeled using a Chebychev polynomial approximation of 6th order. The peak profile was described by a pseudo-Voight. The coefficients of thermal expansion tensor and the orientation of the principal axes of the thermal-expansion tensor with respect to the crystallographic axes were determined using the TEV program [41].

2.4. Spectroscopy Study

In order to obtain infrared (IR) absorption spectra of potassic-hastingsite, powdered samples were mixed with anhydrous KBr, pelletized, and analyzed using an FT-801 spectrometer (Simex, Novosibirsk, Russia) at a resolution of 2 cm^{-1}. A total of 32 scans were collected for each spectrum. The IR spectrum of an analogous pellet of pure KBr was used as a reference.

Diffuse-light absorption spectra in the ultraviolet (UV), visible (Vis) and near infrared (NIR) spectral region were recorded at room temperature with a PerkinElmer Lambda 950 spectrophotometer (Perkin-Elmer, Shelton, CT, USA) in an integrating sphere. For measurements, the powder samples of potassic-hastingsite were placed in a quartz test tube, which is transparent in the range of 250–2000 nm.

Electron spin resonance (ESR) spectra were registered using a RE-1306 X-band spectrometer (KBST, Smolensk, Russia) with a frequency of 9.310 GHz. Powder of potassic-hastingsite was placed in a quartz test tube. The measurements were carried out at room temperature.

3. Results

3.1. Petrographic Analysis

The investigation of the morphogenetic features of potassic-hastingsite and its paragenetic associations allowed us to determine the sequence of the mineral crystallization of the studied skarn sample (Table 3).

Table 3. Schematic diagram showing paragenetic relationships of mineral assemblages in the skarn sample, based on paragenetic relation and microtextural data.

Mineral	Skarn Formation Stages	
	Late Hydrosilicatic Stage	Hydrothermal Stage
Garnet (grossular-andradite)	———	
Apatite	———	
Amphibole (potassic-hastingsite)	———	
Calcite	———	
Vesuvianite1	———	
Quartz		———
Vesuvianite2		———
Sulfides	———	———
Epidote		———
Zoisite		———

3.2. Chemical Composition and Structure Description

Combined EPMA (determined over 16 spots) and XRF results obtained for the studied potassic-hastingsite sample are reported in Table 4, compared with those in the literature for the hastingsites. The results of the XRF show that the Fe^{2+} is the principal oxidation state in the mineral (Fe^{2+} = 74%). The empirical formula was calculated based on fixing the sum of O + OH + Cl + F to 24 by means of the amphibole classification spreadsheet (August 2020 version) originally published by [42]. The formula is represented in Table 5, where the information on the literature crystal chemistry of hastingsites is also summarized.

Table 4. Combined EPMA and XRF data of studied potassic-hastingsite. For comparison purpose, reference data are reported. Hs—hastingsite. n.d.—not determined, b.d.l.—below detection limit.

Constituent	K-Hs, Kedrovy District, Russia This study	K-Hs, Yukon, Canada [7]	K-Hs, Keshiketeng Banner, China [10]	K-Hs, Vlastějovice, Czech Republic [9]	K-Hs, West Ongul Island, East Antarctica [8]	K-Cl-Hs, Dashkesan, Azerbaidjan [13]	K-F-Hs, Greenwood mine, USA [11]	Mg-Hs, Lafarge Quarry, Canada [16]	Mg-F-Hs, Eifel, Rheinland-Pfalz, Germany [20]	Mg-F-Hs, Uroi Hill, Romania [19]	K-Mg-Hs, Ylmenogorsky Complex, South Urals, Russia [18]	K-Mg-Hs, Prince Olav Coast, East Antarctica [17]	O-Mg-Hs, Deeti Volcanic Cone, Northern Tanzania [21]
SiO_2	36.62(63)	37.36(46)	35.02	37.32	35.52	35.62	40.49	39.53	40.02	40.77	36.28	39.43	41.89
Al_2O_3	10.64(8)	11.60(30)	10.69	12.70	11.94	11.13	10.29	14.61	11.81	13.11	16.37	14.31	10.75
Na_2O	0.96(9)	1.27(20)	0.06	1.07	0.80	1.07	1.24	1.99	2.45	1.79	1.05	0.96	2.84
MgO	0.96(8)	0.98(26)	0.23	3.83	4.44	2.91	6.68	14.07	15.24	18.70	10.23	9.02	14.79
K_2O	2.21(10)	2.15(14)	2.79	3.05	3.27	3.04	2.93	2.25	1.60	1.17	3.34	3.07	1.74
CaO	11.05(9)	11.28(22)	11.35	11.38	11.32	10.72	11.13	11.89	12.28	13.99	11.84	12.23	11.76
TiO_2	0.20(8)	0.29(9)	0.35	0.43	0.77	0.43	0.11	3.64	5.38	1.21	1.47	1.03	3.96
$V2O_3$	n.d.	n.d.	n.d.	n.d.	n.d.	n.d.	0.03	n.d.	b.d.l.	n.d.	b.d.l.	n.d.	trace
Cr_2O_3	b.d.l.	0.08(9)	0.03	n.d.	n.d.	n.d.	0.01	0.03	b.d.l.	n.d.	n.d.	0.02	trace
MnO	0.37(6)	0.37(12)	0.43	0.18	0.30	0.40	0.20	0.09	b.d.l.	n.d.	0.45	0.45	0.08
FeO	27.66(52)	25.70(2)	26.08	20.81	19.73	23.48	19.80	5.45	n.d.	n.d.	8.76	8.38	n.d.
Fe_2O_3	6.92(51)	6.55(2)	7.33	6.64	7.44	7.80	4.49	4.76	9.16	6.44	7.29	9.88	11.25
BaO	n.d.	n.d.	n.d.	n.d.	n.d.	n.d.	n.d.	n.d.	b.d.l.	n.d.	0.92	n.d.	n.d.
F	0.17(5)	n.d.	0.00	0.35	0.19	0.14	2.23	0.09	2.36	4.39	n.d.	0.20	n.d.
Cl	2.08(17)	2.35(39)	2.79	0.24	3.27	4.68	0.61	0.02	b.d.l.	n.d.	0.5	0.10	n.d.
Sum	99.84	99.98	97.15	98.00	98.99	101.42	100.24	98.42	100.3	101.57	98.50	99.08	99.06
O = F2	0.07	-	-	0.15	0.82	1.12	1.08	0.04	-0.99	1.84	-	0.11	-
O = Cl	0.47	0.53	0.67	0.05					-	-	0.1		-
Total	99.30	99.45	96.48	97.80	98.17	100.30	99.16	98.38	99.31	99.73	98.40	98.97	99.06

Table 5. Crystal chemical formulae and cation and anion distribution of the studied and literature hastingsite minerals, $AB_2C_5T_8O_{22}W_2$. **A**—A site (pfu); **B**—2 × M4 site (pfu (per formula unit)); **C**—2 × M1, 2 × M2, 1 × M3 sites (pfu); **T**—4 × T1, 4 × T2 sites (pfu); **W**—2 × O3 sites (pfu). The abbreviations of hastingsite species used are the same as in Table 1.

Mineral	A	B	C	T	O	W
K-Hs, Kevrovy district, Russia This study	$K_{0.46}Na_{0.29}$	$Ca_{1.95}Na_{0.03}Mn_{0.02}$	$Fe^{2+}_{3.49}Fe^{3+}_{1.15}Mg_{0.24}Al_{0.06}Mn_{0.04}Ti_{0.02}$	$Si_{6.01}Al_{1.99}$	O_{22}	$(OH)_{1.33}Cl_{0.58}F_{0.09}$
K-Hs, Yukon, Canada [7]	$K_{0.45}Na_{0.40}$	$Ca_{1.97}Na_{0.03}$	$Fe^{2+}_{3.51}Fe^{3+}_{0.81}Al_{0.32}Mg_{0.24}Mn_{0.05}Ti_{0.03}Cr_{0.01}$	$Si_{6.09}Al_{1.91}$	O_{22}	$(OH)_{1.38}Cl_{0.62}$
K-Hs, Keshiketeng Banner, China [10]	$K_{0.61}Na_{0.20}Ca_{0.07}$	$Ca_{2.00}$	$Fe^{2+}_{3.72}Fe^{3+}_{0.94}Al_{0.12}Mg_{0.06}Mn_{0.06}Ti_{0.04}Ni_{0.01}$	$Si_{5.97}Al_{2.03}$	O_{22}	$(OH)_{1.14}Cl_{0.86}$
K-Hs, Vlastějovice, Czech Republic [9]	$K_{0.62}Na_{0.28}$	$Ca_{1.95}Na_{0.05}$	$Fe^{2+}_{2.79}Mg_{0.92}Fe^{3+}_{0.80}Al_{0.38}Ti_{0.05}Mn_{0.03}$	$Si_{5.98}Al_{2.02}$	O_{22}	$(OH)_{1.71}F_{0.18}Cl_{0.06}$
K-Hs, West Ongul Island, East Antarctica [8]	$K_{0.69}Na_{0.26}$	$Ca_{1.99}$	$Fe^{2+}_{2.71}Mg_{1.09}Fe^{3+}_{0.92}Al_{0.15}Ti_{0.10}Mn_{0.04}$	$Si_{5.84}Al_{2.16}$	O_{22}	$(OH)_{0.95}Cl_{0.91}F_{0.10}O_{0.04}$
K-Cl-Hs, Dashkesan, Azerbaidjan [13]	$K_{0.64}Na_{0.34}$	$Ca_{1.90}$	$Fe^{2+}_{3.25}Fe^{3+}_{0.97}Mg_{0.72}Mn_{0.06}Al_{0.06}Ti_{0.05}$	$Si_{5.89}Al_{2.11}$	O_{22}	$Cl_{1.31}(OH)_{0.60}F_{0.07}O_{0.02}$
K-F-Hs, Greenwood mine, USA [11]	$K_{0.59}Na_{0.25}$	$Ca_{1.87}Na_{0.13}$	$Fe^{2+}_{2.60}Mg_{1.56}Fe^{3+}_{0.53}Al_{0.26}Mn_{0.03}Ti_{0.01}$	$Si_{6.36}Al_{1.64}$	O_{22}	$F_{1.11}(OH)_{0.73}Cl_{0.16}$
Mg-Hs, Lafarge Quarry, Canada [16]	$Na_{0.57}K_{0.42}Ca_{0.01}$	$Ca_{1.88}Fe^{2+}_{0.11}Na_{0.02}Mn_{0.01}$	$Mg_{3.10}Fe^{2+}_{0.57}Fe^{3+}_{0.53}Ti_{0.41}Al_{0.39}Mn_{0.02}$	$Si_{5.85}Al_{2.15}$	O_{22}	$(OH)_{1.36}O_{0.59}F_{0.04}Cl_{0.01}$
Mg-F-Hs, Eifel, Rheinland-Pfalz, Germany [20]	$Na_{0.65}K_{0.30}$	$Ca_{1.95}Na_{0.05}$	$Mg_{3.36}Fe^{3+}_{0.87}Fe^{2+}_{0.13}Ti_{0.60}$	$Si_{5.92}Al_{2.08}$	O_{22}	$F_{1.11}O_{0.89}$
Mg-F-Hs, Uroi hill, Romania [19]	$Na_{0.50}K_{0.22}Ca_{0.17}$	$Ca_{2.00}$	$Mg_{4.03}Fe^{3+}_{0.70}Al_{0.13}Ti_{0.13}$	$Si_{5.89}Al_{2.11}$	O_{22}	$F_{2.00}$
K-Mg-Hs, Ylmenogorsky complex, South Urals, Russia [18]	$K_{0.65}Na_{0.31}Ba_{0.04}$	$Ca_{1.93}Mn_{0.06}Ba_{0.01}$	$Mg_{2.32}Fe^{2+}_{1.12}Fe^{3+}_{0.84}Al_{0.47}Ti_{0.17}$	$Si_{5.53}Al_{2.47}$	O_{22}	$(OH)_{1.93}Cl_{0.13}$
K-Mg-Hs, Prince Olav Coast, East Antarctica [17]	$K_{0.85}Na_{0.11}Ca_{0.02}$	$Ca_{1.98}Mn_{0.02}$	$Mg_{1.92}Fe^{2+}_{1.20}Fe^{3+}_{1.11}Al_{0.64}Ti_{0.13}Mn_{0.01}$	$Si_{5.64}Al_{2.36}$	O_{22}	$(OH)_{1.36}O_{0.48}F_{0.12}Cl_{0.04}$
O-Mg-Hs, Deeti volcanic cone, Northern Tanzania [21]	$Na_{0.67}K_{0.33}$	$Ca_{1.87}Na_{0.14}Mn_{0.01}$	$Mg_{3.27}Fe^{3+}_{1.25}Ti_{0.44}Al_{0.08}$	$Si_{6.20}Al_{1.80}$	O_{22}	$O_{1.40}(OH)_{0.60}$

The projection of the crystal structure parallel to the *a*-axis is shown in Figure 4. The potassic-hastingsite structure is based on the infinite chain of T_4O_{11} anions. The six-coordinated C cations sandwiched between two chains occupy the positions marked *M*1, *M*2, and *M*3, arranging as a strip. The B cations occupy the *M*4 positions at the edge of the whole tetrahedral-octahedral complex. The A cations lie between the backs of the chains.

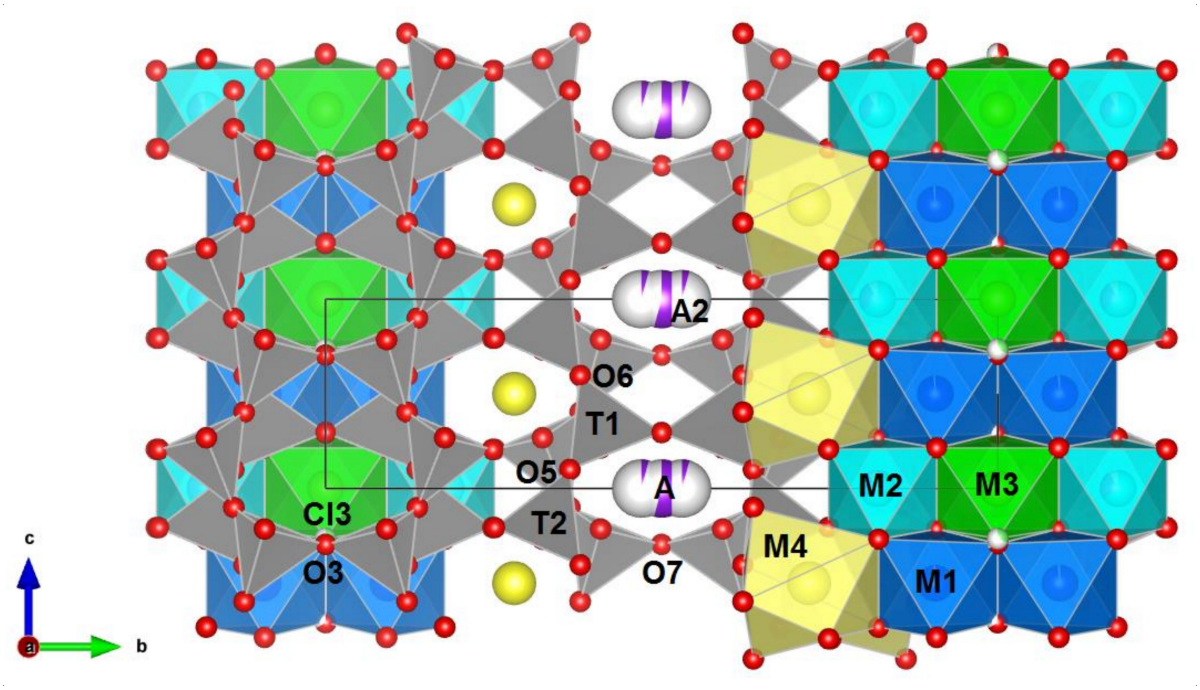

Figure 4. Crystal structure of potassic-hastingsite projected along the *a* axis. Oxygen atoms are drawn in red. Si-tetrahedra and mixed Si-Al tetrahedra are gray. *M*1—blue, *M*2—cyan, *M*3—green octahedra, *M*4—yellow polyhedra. A and A2 positions are designated as lilac spheres. Cl3 sites are drawn in light green. The partially white coloring of the spheres indicates a vacancy. The relations between the ribbon of octahedra and the double-chain tetrahedra are shown.

The unit-cell dimensions for studied single crystal of potassic-hastingsite are a = 9.9724(3) Å, b = 18.2968(4) Å, c = 5.3573(1) Å, β = 104.945(3)°, V = 944.44(4) Å^3, Z = 2. Final atomic coordinates, site occupancies, and equivalent and anisotropic displacement parameters are reported in Table 6 and Table S1 of the Supplementary Materials. In Table 7, selected bond lengths, angles, and distortion parameters describing the coordination polyhedra for the studied sample are provided.

Table 6. Crystallographic coordinates, occupancies, and equivalent/isotropic atomic displacement parameters (Å^2) of the studied potassic-hastingsite sample.

Site	Atom	*x/a*	*y/b*	*z/c*	Occ.	Ueq
A	K^+	0	0.5	0	0.524(1)	0.0499
*A*2	K^+	0	0.4728(7)	0	0.037(1)	0.0499
*M*1	Fe^{2+}	0	0.09259(2)	0.5	1	0.0144
*M*2	Fe^{2+}, Fe^{3+}, Mg^{2+}	0	0.17915(2)	0	0.99(1)	0.119
*M*3	Fe^{2+}	0	0	0	1	0.0136
*M*4	Ca^{2+}	0	0.28067(2)	0.5	1	0.0158
*T*1	Si^{4+}, Al^{3+}	0.27837(4)	0.08558(2)	0.29999(8)	1	0.0110
*T*2	Si^{4+}	0.29083(4)	0.17265(2)	0.80998(7)	1	0.0108
O1	O^{2-}	0.1057(1)	0.09079(6)	0.2138(2)	1	0.0143
O2	O^{2-}	0.1218(1)	0.17736(6)	0.7320(2)	1	0.0138
O3	O^{2-}, F^-	0.1092(5)	0	0.7087(4)	0.68(1)	0.0135
	Cl^-	0.1623(2)	0	0.7358(3)	0.31(1)	0.0154

Table 6. *Cont.*

Site	Atom	*x*/*a*	*y*/*b*	*z*/*c*	Occ.	Ueq
O4	O^{2-}	0.3688(1)	0.24841(6)	0.7935(2)	1	0.0159
O5	O^{2-}	0.3467(1)	0.13651(6)	0.1003(2)	1	0.0155
O6	O^{2-}	0.3423(1)	0.12116(6)	0.5967(2)	1	0.0162
O7	O^{2-}	0.3331(2)	0	0.2953(3)	1	0.0195

Table 7. Selected bond distances (Å), angles and calculated geometrical and distortion parameters for tatrahedra, octahedra and polyhedra in the crystal structure of the studied potassic-hastingsite sample. The volume of the coordination tatrahedra, octahedra and polyhedra (Vt, Vo and Vp), as well as bond length distortion (BLD), tetrahedral and octahedral angle variance (TAV and OAV) and tetrahedral and octahedral quadratic elongation (TQE and OQE) were calculated using VESTA (version 4.3.0) [39] according [43,44].

***T*1 Site**		***T*2 Site**		***A* Site**	
*T*1-O1	1.667(1)	*T*2-O2	1.631(1)	*A*-O5 (×4)	3.048(1)
*T*1-O5	1.689(1)	*T*2-O4	1.603(1)	*A*-O6 (×4)	3.210(1)
*T*1-O6	1.684(1)	*T*2-O5	1.650(1)	*A*-O7 (×2)	2.576(2)
*T*1-O7	1.660(1)	*T*2-O6	1.661(1)	<*A*-O>	3.018(3)
<*T*1-O>	1.675(3)	<*T*2-O>	1.636(4)		
				Vp (Å^3)	50.300
O1-*T*1-O5	110.49(5)	O2-*T*2-O4	115.13(6)	BLD (%)	5.866
O1-*T*1-O6	110.59(6)	O2-*T*2-O5	109.73(6)	***A*2 site**	
O1-*T*1-O7	111.71(7)	O2-*T*2-O6	109.64(6)	A2-O5 (×2)	2.614(25)
O5-*T*1-O6	105.54(8)	O4-*T*2-O5	110.36(6)	A2-O6 (×2)	2.856(19)
O5-*T*1-O7	108.85(7)	O4-*T*2-O6	102.27(6)	A2-O7 (×2)	2.635(7)
O6-*T*1-O7	109.44(7)	O5-*T*2-O6	109.39(6)	<A2–O>	2.702(48)
<O-*T*1-O>	109.4(2)	<O-*T*2-O>	109.4(1)	***M*3 site**	
				*M*3-O1 (×4)	2.135(1)
*T*1-O7-*T*1	141.15(12)	*T*1-O5-*T*2	136.49(7)	*M*3-O3 (×2)	2.121(4)
				*M*3–Cl3 (×2)	2.409(3)
Vt (Å^3)	2.407	Vt (Å^3)	2.233	<*M*3-O_6>	2.130(5)
BLD (%)	0.684	BLD (%)	1.176	<*M*3-O_5Cl>	2.178(3)
TAV	4.6077	TAV	16.9950	<*M*3-O_4Cl_2>	2.226(5)
TQE	1.0011	TQE	1.0044	***M*4 site**	
***M*1 site**		***M*2 site**		*M*4-O2 (×2)	2.412(1)
*M*1-O1 (×2)	2.073(1)	*M*2-O1 (×2)	2.101(1)	*M*4-O4 (×2)	2.351(1)
*M*1-O2 (×2)	2.156(1)	*M*2-O2 (×2)	2.107(1)	*M*4-O5 (×2)	2.744(1)
*M*1-O3 (×2)	2.163(1)	*M*2-O4 (×2)	1.986(1)	*M*4-O6 (×2)	2.527(1)
*M*1–Cl3 (×2)	2.456(1)	<*M*2-O>	2.065(3)	<*M*4-O>	2.508(3)
<*M*1-O_6 >	2.131(3)				
<*M*1-O_5Cl>	2.180(3)	Vo (Å^3)	11.611	Vp (Å^3)	26.509
<*M*1-O_4Cl_2>	2.228(3)	BLD (%)	2.532	BLD (%)	5.069
		OAV	23.3661		
*M*1–*M*2	3.1119(2)	OQE	1.0078	*A*–*A*2	0.498(13)
*M*1–*M*3	3.1694(2)			*A*2–*A*2	1.00(3)
*M*2–*M*3	3.2779(4)			O3–Cl3	0.511(3)

3.3. In Situ HTXRPD

Initial cell dimensions obtained from the powder data refinement are as follows: a = 9.975(2) Å, b = 18.282(5) Å, c = 5.364(2) Å, β = 104.97(3)°, and V = 944.9(4) Å^3 (at 30 °C), and are closed to those derived from SCXRD data. The unit cell parameters calculated at each step of heating and cooling are given in Table S2 of the Supplementary Materials. The color of the potassic-hastingsite powder changed from dark green to brown after the experiment.

On heating and cooling from 30 to 750 °C and back to 30 °C, the peaks positions in the diffraction patterns changed smoothly (Figures S1 and S2, Table S3 of the Supplementary Meterials). The evolution of the unit cell parameters and volume of potassic-hastingsite as a function of temperature is plotted in Figures 5 and 6.

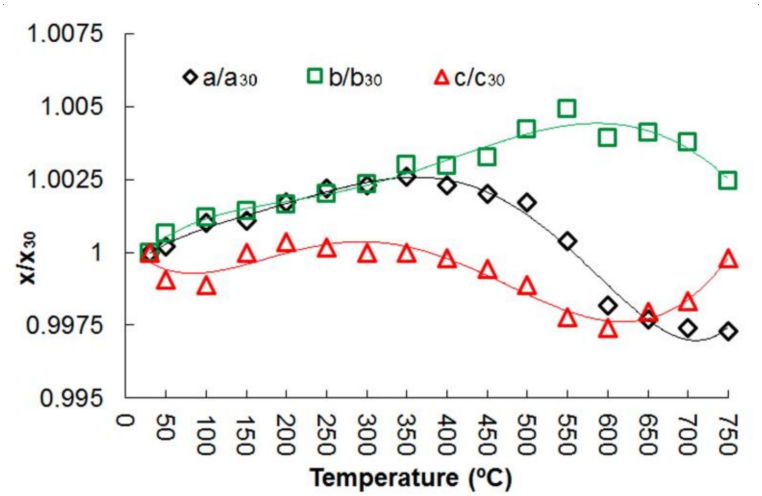

Figure 5. Normalized unit cell parameters of potassic-hastingsite *vs* temperature. Symbols: a/a_{30}—black diamonds; b/b_{30}—green squares; c/c_{30}—red triangles. Estimated standard deviations are smaller than the symbol used. A fifth-order polynomial approximation has been used for trend lines.

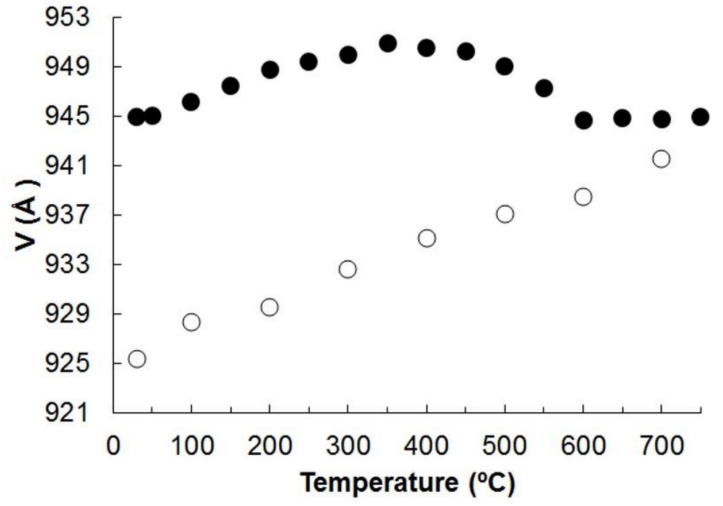

Figure 6. Unit cell volume of potassic-hastingsite *vs* temperature. Symbols: solid for the heating experiment; empty for the cooling. Estimated standard deviations are smaller than the symbol used.

The coefficients of thermal expansion tensor and the orientation of the principal axes of the thermal-expansion tensor with respect to the crystallographic axes are listed in Table S4 of the Supplementary Materials. A fifth-order polynomial approximation of temperature dependencies has been used.

3.4. Spectroscopy

Infrared absorption spectra of initial and annealed at 750 °C potassic-hastingsite are shown in Figure 7. Weak bands peaked at 595, 660, 739, 3610 cm^{-1} and strong bands at 877, 935, 968, and 1049 cm^{-1} were observed in the initial potassic-hastingsite. During annealing most changes occur in the range 550–750 cm^{-1}. Two bands near 595 and 730 cm^{-1} start to displace after heating to 550 °C together with the OH stretching band at 3610 cm^{-1} and disappear after sample heating at temperatures higher than 650 °C. The OH-stretching

band demonstrates the same temperature behavior. A weak intensity band at 684 cm^{-1} is not retired, but it is displaced at 660 cm^{-1} during sample heating. The absorption spectrum of the sample that was annealed at 750 °C is given in Figure 7 (curve 2).

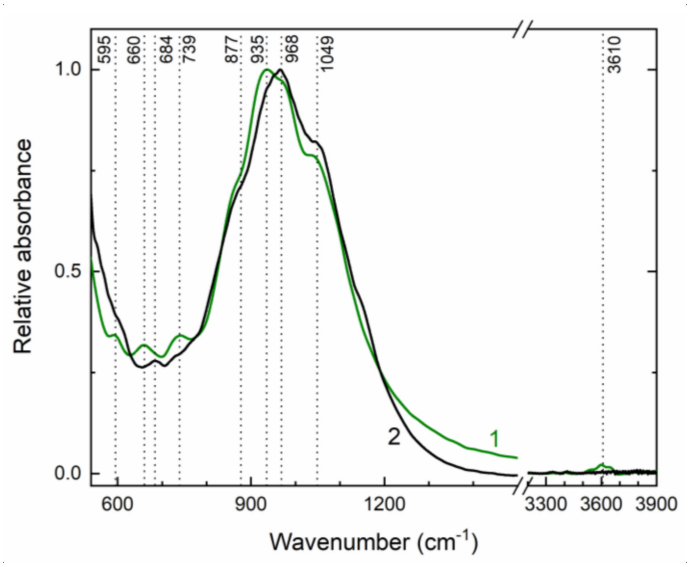

Figure 7. Infrared absorption spectra of initial (green curve 1) and annealed at 750 °C (black curve 2) potassic-hastingsite.

In the UV/Vis/NIR absorption spectrum of initial potassic-hastingsite, strong structureless bands at the 800–1600 nm spectral region are observed (Figure 8, curve 1). In addition, a moderate-intensity band in the range 520–800 nm is found. After annealing at 750 °C the absorption spectrum is changed. The strong band grows in the 250–600 nm spectral region, but the bands in the 800–1600 nm spectral region and at about 680 nm are decreased (Figure 8, curve 2).

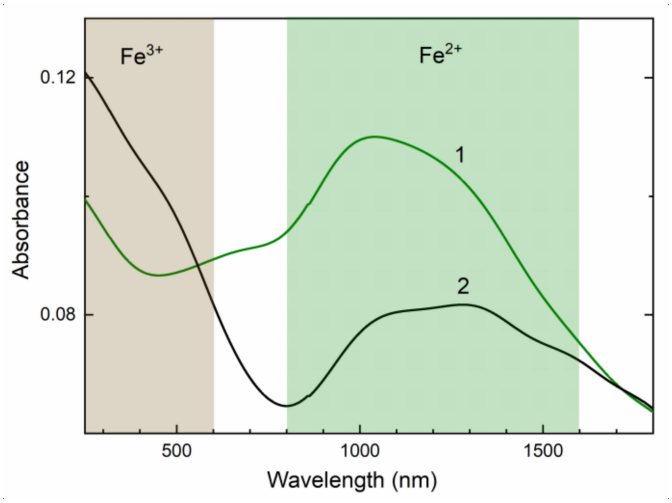

Figure 8. Diffuse light UV/Vis/NIR absorption spectra of initial (green curve 1) and annealed (black curve 2) potassic-hastingsite.

A strong ESR signal is detected at room temperature. ESR spectrum of the initial potassic-hastingsite is shown in Figure 9 (curve 1). Strong wide peaks with g-factors 4.2 and 2.01 are found in the spectrum. In the annealed at 750 °C sample, the intensity of the ESR signal is increased and changed in comparison with the initial sample (Figure 9, curve 2). Strong wide bands have g-factors at about 2.3 and 1.9. The relationship between the spectra of the annealed and the initial samples is shown in the inset to Figure 9.

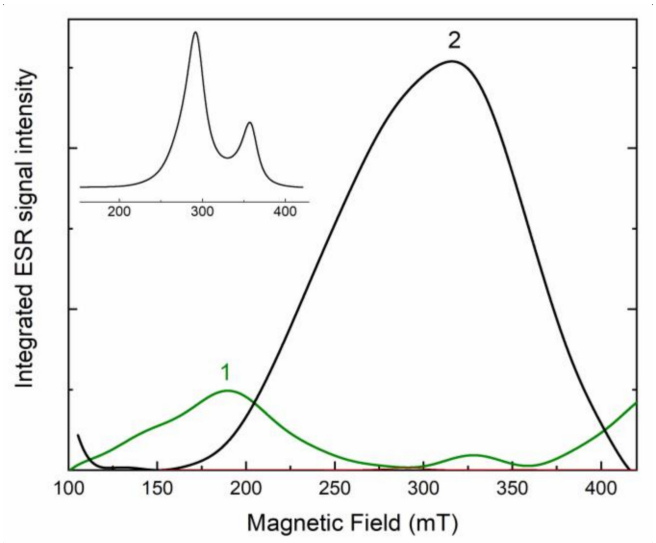

Figure 9. Electron spin resonance spectra of initial (green curve 1) and annealed (black curve 2) potassic-hastingsite. The ratio of curve 2 to curve 1 is given in the inset to the Figure.

4. Discussion

4.1. Chrystal Chemical Features

Table 8 yields the results of a bond-valence analysis for the studied sample. Analysis of Table 8 reveals that the bond-valence sums (BVS) are generally satisfactory for the oxygen atoms. A disordering of the anionic O3 site over two positions partially occupied by OH-group and Cl ion is observed. The O3 site has a low bond-valence sum (1.0 vu (valence units)), leading to the conclusion that it is populated with $(OH)^-$ and $F^-$and does not contain O^{2-} atoms.

Table 8. Bond-valence sum for the studied potassic-hastingsite using the parameters by [45,46].

	*T*1	*T*2	*A*	*A*2	*M*1	*M*2	*M*3	*M*4	∑
O1	0.897				$0.395^{[\times 2]}$	$0.371^{[\times 2]}$	$0.344^{[\times 4]}$		2.007
O2		0.984			$0.328^{[\times 2]}$	$0.366^{[\times 2]}$		$0.291^{[\times 2]}$	1.969
O3					$0.323^{[\times 2]\,(\times 2)}$		$0.355^{[\times 2]}$		1.001
Cl3					$0.343^{[\times 2]\,(\times 2)}$		$0.389^{[\times 2]}$		1.075
O4		1.055				$0.480^{[\times 2]}$		$0.337^{[\times 2]}$	1.872
O5	0.847	0.936	$0.081^{[\times 4]}$	$0.241^{[\times 2]}$				$0.129^{[\times 2]}$	1.993–2.153
O6	0.858	0.909	$0.054^{[\times 4]}$	$0.131^{[\times 2]}$				$0.219^{[\times 2]}$	2.040–2.117
O7	$0.912^{(\times 2)}$		$0.265^{[\times 2]}$	$0.228^{[\times 2]}$					2.089–2.052
∑	3.515	3.884	1.070	1.200	2.092–2.132	2.434	2.086–2.154	1.952	

$^{[\times 2]}$, $^{[\times 4]}$: for the calculation of the valence bond sum for cations. $^{(\times 2)}$: for the calculation of the valence bond sum for anions.

A cations. The A cations occur at the center of a large cavity between the two tetrahedral chains, oriented back-to-back with respect to each other. In the crystal structure of the studied sample, A cation site is partially populated by K and Na. It should be noted that the A cation position in the studied structure is split.

B cations. Ca and minor Na and Mn (1% of the total occupancy for each, Table 5) are located at the B cations formula site and the *M*4 structural position, within the eight-coordinated polyhedron. The bond valence sum for the atoms at *M*4 positions is almost 2 (Table 8).

C cations. The octahedral *M*1, *M*2, and *M*3 cation sites are mainly occupied by Fe^{2+} and Fe^{3+} with minor amounts of Mg, Al, Mn, and Ti. The BVS of of *M*1 and *M*3 sites equals ~2.1 vu (Table 8), whereas the sum of the bond valence at the *M*2 site is 2.43 vu (i.e., 2 < vu < 3; Table 8) and the average *M*2-O distance is 2.065(3) Å (Table 7) which gives grounds to assume that Fe enters the *M*2 of the crystal structure in both two- and three-

valent form, as expected based on previous literature. This polyhedron is also noted by slightly lower octahedral volume and BLD parameter and slightly greater OAV (octahedral angle variance; [43]) distortion (see Table 7). Fe^{2+} occupies *M*1 and *M*3 positions, forming Fe^{2+}–Cl^{-} pairs, as reported by [47]. Oberti et al. (2007) have reported crystal-chemical relationships, which allow calculation of the oxo component using the refined *M*1–*M*2 distance in calcium amphiboles [37]. This method provides 0.6 $^{W}O^{2-}$ apfu for studied structural model with *M*1–*M*2 = ~3.11 Å (Table 7). However, O3 position splitting and significant ^{M2}Mg content might affect the experimental interatomic distances and lead to higher estimates of the oxo component, which is inconsistent with the values calculated using the EPMA analysis.

T cations. The measured *T*–O individual distances range from 1.660(1) to 1.689(1) and from 1.603(1) to 1.661(1) for *T*1 and *T*2 sites, respectively. On the basis of observed <*T*–O> distances (Table 7), it is possible to state that the *T*1 position (<*T*1–O> ~ 1.68 Å; tetrahedral volume, Vt, is equal to 2.41 $Å^3$; BVS ~ 3.5 vu) has mixed occupancy (Al ~ 1.91 apfu according to the equation published by [37]); whereas the *T*2 site (<*T*2–O> ~ 1.64 Å; Vt ~ 2.23 $Å^3$; BVS ~ 3.9 vu) is fully filled by Si^{4+} ion, which is a common for monoclinic amphiboles [48]. The BLD values for *T*1 and *T*2 tetrahedra are ~0.68% and ~1.18%, respectively, and the TAV (tetrahedral angle variance; [44]) values are ~4.61 and ~17.00, respectively (Table 7).

4.2. Thermal Behavior and Spectroscopic Properties

No evidence of phase transition was observed within the T range investigated and all the diffraction patterns were successfully indexed in the *C*2/*m* space group. The unit cell volume variation as a function of T is shown in Figure 6. The measured evolution of the unit cell parameters is shown in Figure 5.

The thermal expansion of potassic-hastingsite is anisotropic. The graphical representation of the thermal expansion of the potassic-hastingsite is displayed in Figures S3–S7 of the Supplementary Materials. At T = 100–300 °C the mineral exhibits a positive expansion for all the directions (Figure 6 and Figure S3 of the Supplementary Materials) (the thermal expansivity coefficients are α_a:α_b:α_c ($\times 10^{-6}$) = 2.34:9.26:1.15 at 100 °C and −0.75:7.11:5.58 at 300 °C), while a shrinkage along the [101] direction occurs at T = 350 °C (Figure S4 of the Supplementary Materials). The thermal expansivity coefficients are α_a:α_b:α_c ($\times 10^{-6}$) = −9.41:8.71:2.32 at 350 °C. In the temperature range 400–600 °C potassic-hastingsite shows a strong negative thermal expansion (Figure 6 and Figures S5 and S6 of the Supplementary Materials). The thermal expansivity coefficients are α_a:α_b:α_c ($\times 10^{-6}$) = −18.06:9.59:−1.09 at 400 °C and −26.15:−1.52:2.22 at 600 °C. Starting from 600 °C, the mineral expands again preferentially along [001] and shrinks along [110] without changes in the volume of unit cell (Figure 6 and Figure S7 of the Supplementary Materials). The thermal expansivity coefficients are α_a:α_b:α_c ($\times 10^{-6}$) = −20.86:−8.33:−10.56 at 650 °C and 23.77:−25.06:42.08 at 750 °C.

A closer comparison between the elastic properties of potassic-hastingsite can be made with amphiboles, Fe-rich holmquistite, riebeckite, investigated by [49] and [50,51], respectively, and synthetic potassic-ferro-richterite, studied by [52,53].

Oberti et al. (2018) reported that oxidation of Fe^{2+} and the consequent deprotonation at the O3 site causing the reduction of all unit cell parameters and volume in riebeckite starts at ∼350–425 °C [50]. The temperature of the onset of deprotonation of potassic-ferro-richterite is even lower (∼226 °C; [52]). According to [50] and [52], iron oxidation in riebeckite and potassic-ferro-richterite takes place almost exclusively at the *M*(1) site despite the fact that both the *M*1 and *M*3 polyhedra coordinate (OH)-anion at the O3 site.

In the range 30–350 °C, our sample of potassic-hastingsite shows positive and linear expansion, with a small contraction of the *c* parameter and β angle. Taking into account the results of previous studies of monoclinic Fe^{2+}– and Fe^{3+}–containing amphiboles [50,52], we concluded that the oxidation of Fe occurs in the temperature range of 400–600 °C when the unit cell volume decreases; then the *c* parameter expands again (Figures 5 and 6). This value is somewhat higher than that observed for the aforementioned amphiboles.

During the heating of studied potassic-hastingsite Fe^{2+} in the M1 position oxidizes to Fe^{3+}, meanwhile H_2 is released from the O3 site, common for two M1 and one M3 octahedra.

The *a* edge is very sensitive to thermal expansion, followed by the *b* edge (Figure 5). Moreover, the *a* edge is the most sensitive to deprotonation (Figure 5). It can be noted that the thermal expansion process is completed at about 350 °C, and after that the compression process of *a* and *c* unit cell parameters begins. After passing a temperature of 600 °C, the *c* increases again.

The sharp band at 3610 cm^{-1} on the IR spectrum (Figure 7) is assigned to the local configuration of $^{M1}Fe^{2+}\,^{M1}Fe^{2+}\,^{M3}Fe^{2+}$ -OH—A vacancy [54,55]. This band indicated that the studied amphibole has an ordered structure, having Fe^{2+} in the M1 and M3 positions and Fe^{3+} in the M2 position [56,57]. This spectroscopic data confirm the conclusions obtained from the SCXRD study and represented in Table 6.

The 595 and 730 cm^{-1} bands disappear in the IR spectrum of the annealed potassic-hastingsite. Their destruction is accompanied by a decrease in the intensity of the peak in the 3610 cm^{-1} region associated with the OH stretching vibrations. Thus, it can be assumed that the hydroxyl anion is also involved in the vibrations associated with the 595 and 730 cm^{-1} bands, and the deprotonation was complete. Early Ishida (1990) founded a broad or medium intensity OH librational band near 600 cm^{-1} in A site-occupied and Al(IV)-free amphiboles [58]. Sergeeva et al. (2020) pointed, that the infrared bands at 740 and 725 cm^{-1} correspond to librational vibrations of water coordinated to Al [59]. Generally, libration modes have been discussed in more detail by us in [60].

A medium intensity band at 684 cm^{-1} could be ascribed assigned to O_{nbr}-Si-O_{nbr} bending deformations following Ca- and other amphiboles [61]. The frequency of this band significantly depends on the octahedral cations and the distance between cation and O2 [58]. Therefore, after the high-temperature experiment the unit cell volume is decreased and the frequency of this bending vibration is shifted to the low energy region.

In the visible spectral region, the amphibole, cordierite, and sekaninaite absorption spectra display an intense pleochroic band located at about 580–750 nm attribute to Fe^{2+}/Fe^{3+} intervalence charge transfer transition (IVCT) [62,63]. This charge transfer transition occurs between intervalence Fe pairs due to delocalization of the d-electron along Fe^{2+}–Fe^{3+} bond.

Near-infrared absorption (NIR) bands are attributed to dd transitions in Fe^{2+} ions. The Fe^{2+} ion has a d^6 electron configuration. In octahedral amphiboles absorption at about 1000 nm is due to transition in Fe^{2+} cations in position M1 (Figure 8). Longer wavelength absorption bands at 1300 and 1600 nm are also found in Ca-amphiboles. They are caused by spin-allowed dd transition of Fe^{2+} in M2 and M3 sites [62,64].

In the annealed sample, the band in the region 250–600 nm appears (Figure 8). This absorption is assigned to dd transition in octahedral coordinated Fe^{3+} ions [65]. This is also led to changing the color of the potassic-hastingsite from green to brown.

Obtained ESR spectra are attributed to Fe^{3+} ions. In the initial sample, the ESR signal (Figure 9) with g-factors 2.01 and 4.2 corresponds to Fe^{3+} in a low spin octahedral position. The lines are highly broadened due to the exchange interaction between Fe ions [66]. In the annealed sample, the ESR signal is increased due to the appearance of two new components with g-factors 1.9 and 2.3 (Figure 9). A similar signal is usually registered for Fe^{3+} in high spin states in octahedral crystal field [67]. This fact is evidence that Fe^{3+} cations appear in new coordination after annealing of the potassic-hastingsite.

The change of absorption spectra occurs due to a decrease of Fe^{2+} concentration preferably in the M1 site because intensities of 1300 and 1600 bands are retained (Figure 8). At the same time, the concentration of Fe^{3+} cations is increased in the annealed sample. Based on ESR data, the position of these Fe^{3+} cations is the non-equivalent of the one in the initial sample (Figure 9). The diminution of the IVCT band in the 680 nm region corresponds to a decrease of Fe^{2+}/Fe^{3+} pairs.

The removal of OH bands by heating in air suggests that OH^- (Figure 7) is lost through an oxidation-dehydrogenation reaction of the type [68]:

$$Fe^{2+} + OH^- \rightarrow Fe^{3+} + O^{2-} + 1/2H$$

Therefore, the oxidation process leads to an increase in Fe^{3+} in the *M*1 position where the Fe^{2+} cations are located before the heating. This oxidation is confirmed by the optical spectra, which show the decrease in Fe^{2+} content and increase of Fe^{3+} content. Furthermore, Fe^{2+} cations in the *M*1 site participate in Fe^{2+}/Fe^{3+} pairs, which provided an IVCT absorption band. After oxidation of Fe^{2+} IVCT absorption is diminished.

Finally, the values of the cell parameters refined at room temperature after the cooling of the sample are not the same obtained before the direct experiment (see Table S2 of the Supplementary Materials), indicating that the processes occurring in potassic-hastingsite during HT experiments are irreversible. Consistently, the HTXRPD data detect a cell volume decrease of the cooling phase of about 2% with respect to the initial one.

5. Conclusions

Amphiboles are an important supergroup of rock-forming minerals, which crystallize under almost all conditions and have unusually high chemical variability. They play a significant role in a number of metasomatic and metamorphic processes. The chemical diversity originates from their crystal structure, which is able to include a wide range of elements. Because of their importance, a number of mineralogical and spectroscopic investigations and studies at high temperature (HT) are constantly being carried out to describe the crystal-chemical and optical properties, thermoelastic behavior, and deformation mechanisms of the amphiboles.

Crystal chemistry, spectroscopy and thermal behavior of potassic-hastingsite from the Kedrovy district (East Siberia, Russia) with crystal-chemical formula $^{A}(K_{0.46}Na_{0.29})\,^{B}(Ca_{1.95}Na_{0.03}Mn_{0.02})^{C(M1)}(Fe^{2+}{}_{1.96}Mn_{0.04})^{C(M2)}(Fe^{3+}{}_{1.15}Fe^{2+}{}_{0.52}Mg_{0.24}Al_{0.06}Ti_{0.02})^{C(M3)}(Fe^{2+})\,^{T}(Si_{6.01}Al_{1.99})O_{22}\,^{W}(OH_{1.33}Cl_{0.58}F_{0.09})$ were studied and the petrographic description of the amphibole-containing rock sample was carried out.

This is the first study in which the thermal behavior of potassic-hastingsite is described at temperatures up to 750 °C. The study indicates that this mineral undergoes a process of the oxidation of Fe^{2+} and the associated deprotonation that are complete and irreversible. In particular, the thermal experiment indicates that there are two steps of thermal evolution: expansion in the range 30–~350 °C) followed by the structural contraction (~400–600 °C) associated with oxidation of Fe^{2+} to Fe^{3+}, while H_2 is released. The spectroscopic studies confirm this statement. After heating, obtained optical spectra show the decrease in Fe^{2+} content and increase of Fe^{3+} content in the sample. The ESR evidences the appearance of Fe^{3+} in the new structural site.

The study of the mineral composition of the rock sample by petrographic methods makes it possible to assign it to Ca-Fe-Si postmagmatic skarns [69–72]. Paragenetic relationships of grossular-andradite, apatite, potassic-hastingsite, calcite, and vesuvianite (first generation) suggest that they were formed at the late hydrosilicate stage of skarn formation, occurring at temperatures of ~500–400 °C [72–75] (Table 3). The mineral associations of the early stage are superimposed by hydrothermal parageneses: quartz, vesuvianite (second generation), and sulfide veinlets, epidote, and zoisite (Table 3). Thus, at the final hydrothermal stage (temperature ~400–150 °C), the skarn underwent changes. However, the irreversible deprotonation and oxidation of iron, and as a consequence, the color change that occurs when potassic-hastingsite is heated above 400 °C, indicate that after the hydrosilicate and final hydrothermal stages of skarn formation, the rock did not undergo transformations under the influence of temperatures above the specified range. It had a retrograde character. The transformation of sulfides into iron hydroxides took place, most likely, at the supergene stage of rock alteration.

Supplementary Materials: The following are available online at https://www.mdpi.com/article/10.3390/min11101049/s1, Table S1: Anisotropic atomic displacement parameters ($Å^2$) of potassic-hastingsite sample, Table S2: Unit cell parameters of the studied potassic-hastingsite as a function of T, Table S3: X-ray powder diffraction data *vs* temperature for studied potassic-hastingsite, Table S4: Coefficients of thermal expansion tensor (α_{ij}) of the studied potassic-hastingsite as a function of T and orientation of its eigenvectors with respect to unit cell axes, Figure S1: Selected XRPD patterns of potassic-hastingsite showing the evolution of the diffraction patterns collected during the heating experiment, Figure S2: XRPD patterns of potassic-hastingsite showing the evolution of the diffraction patterns collected during the cooling experiment, Figure S3: Graphical representation of the thermal expansion tensor of the potassic-hastingsite at 100 °C, Figure S4: Graphical representation of the thermal expansion tensor of the potassic-hastingsite at 350 °C, Figure S5: Graphical representation of the thermal expansion tensor of the potassic-hastingsite at 400 °C, Figure S6: Graphical representation of the thermal expansion tensor of the potassic-hastingsite at 600 °C, Figure S7: Graphical representation of the thermal expansion tensor of the potassic-hastingsite at 750 °C.

Author Contributions: Conceptualization, E.K.; methodology, E.K. and R.S.; investigation, E.K., T.R., R.S., V.C. and V.D.; writing—original draft preparation, E.K., T.R., R.S. and V.C.; writing—review and editing, E.K.; visualization, E.K., T.R. and R.S. All authors have read and agreed to the published version of the manuscript.

Funding: This research was supported by INRTU, grant number 15-RAS-2020 (Grant of the University Council). XRF and powder XRD were performed by the governmental assignment in terms of Project 0284-2021-0005.

Data Availability Statement: Not applicable.

Acknowledgments: The authors thank the staff of Sidorov Mineralogical Museum of INRTU, who kindly provided the sample studied in this work. The study was carried out using facilities of the Centers for Collective Use: "Center for isotopic-geochemical investigations" at the Vinogradov Institute of Geochemistry SB RAS, "Baikal analytical center for collective use" at the Favorsky Irkutsk Institute of Chemistry SB RAS, and the "Analytical Center for Multielement and Isotope Research" at the Sobolev Institute of Geology and Mineralogy SB RAS. We are grateful to reviewers for their valuable comments.

Conflicts of Interest: The authors declare no conflict of interest.

References

1. Hawthorne, F.C.; Oberti, R. Classification of the amphiboles. *Rev. Mineral. Geochem.* **2007**, *67*, 55–88. [CrossRef]
2. Leake, B.E.; Woolley, A.R.; Arps, C.E.S.; Birch, W.D.; Gilbert, M.C.; Grice, J.D.; Hawthorne, F.C.; Kato, A.; Kisch, H.J.; Krivovichev, V.G.; et al. Nomenclature of amphiboles: Report of the Subcommittee on amphiboles of the International Mineralogical Association Commission on New Minerals and Mineral Names. *Mineral. Mag.* **1997**, *61*, 295–321. [CrossRef]
3. Hawthorne, F.C.; Oberti, R.; Harlow, G.E.; Maresch, W.V.; Martin, R.F.; Schumacher, J.C.; Welch, M.D. Nomenclature of the amphibole supergroup. *Am. Mineral.* **2012**, *97*, 2031–2048. [CrossRef]
4. Adams, F.D.; Harrington, B.J. On a new alkali hornblende and a titaniferous andradite from the nepheline-syenite of Dungannon, Hastings County, Ontario. *Am. J. Sci.* **1896**, *151*, 210–218.
5. Makino, K.; Tomita, K. Cation distribution in the octahedral sites of hornblendes. *Am. Mineral.* **1989**, *74*, 1097–1105.
6. Makino, K.; Tomota, K.; Suwa, K. Effect of chlorine on the crystal structure of a chlorine-rich hastingsite. *Mineral. Mag.* **1993**, *57*, 677–685. [CrossRef]
7. Dick, L.A.; Robinson, G.W. Chlorine-bearing potassian hastingsite from a sphalerite skarn in southern Yukon. *Can. Mineral.* **1979**, *17*, 25–26.
8. Suwa, K.; Enami, M.; Horiuchi, T. Chlorine-rich potassium hastingsite from West Ongul Island, Lutzow-Holm Bay, East Antarctica. *Mineral. Mag.* **1987**, *51*, 709–714. [CrossRef]
9. Žáček, V. Potassium hastingsite and potassichhastingsite from garnet—Hedenbergite skarn at Vlastějovice, Czech Republic. *Neues Jahrb. Mineral.-Abh.* **2007**, *184*, 161–168. [CrossRef]
10. Ren, G.; Li, G.; Shi, J.; Gu, X.; Fan, G.; Yu, A.; Liu, Q.; Shen, G. Potassic-hastingsite, $KCa_2(Fe^{2+}{}_4Fe^{3+})(Si_6Al_6)O_{22}(OH)_2$, from the Keshiketeng Banner, Inner Mongolia, China: Description of the neotype and its implication. *Mineral. Petrol.* **2020**, *114*, 403–412. [CrossRef]
11. Lupulescu, M.V.; Rakovan, J.; Dyar, M.D.; Robinson, G.W.; Hughes, J.M. Fluoro-potassichastingsite from the Greenwood mine, Orange county, New York: A new end-member calcic amphibole. *Can. Mineral.* **2009**, *47*, 909–916. [CrossRef]
12. Krutov, G.A. Dashkesanite—A new chlorine-containing amphibole of the hastingsite group. *Izvest. AN USSR Geol. Ser.* **1936**, *2–3*, 341–373. (In Russian)

13. Pekov, I.V.; Chukanov, N.V.; Nefedova, M.E.; Pushcharovsky, D.Y.; Rastsvetaeva, R.K. Chloro-potassichastingsite (K,Na)Ca_2(Mg,Fe^{2+})$_4$ Fe^{3+}[$Si_6Al_2O_{22}$](OH,Cl)$_2$: Revalidation and the new name of dashkesanite. *Zap. RMO* **2005**, *6*, 31–36. (In Russian)
14. Billings, M. The chemistry, optics and genesis of the hastingsite group of amphiboles. *Am. Mineral.* **1928**, *13*, 287–296.
15. Walitzi, E.M.; Walter, F. Verfeinerung der keistallstruktur eines basaltischen magnesio-hastingsites. *Z. Kristallogr.* **1981**, *156*, 197–208. (In German) [CrossRef]
16. Martin, R.F.; Alarie, É.; Minarik, W.G.; Wáczek, Z.; McCammon, C.A. Titanium-rich magnesio-hastingsite macrocrysts in a camptonite dike, Lafarge quarry, Montreal island, Québec: Early crystallization in a pseudo-unary system. *Can. Mineral.* **2016**, *54*, 65–78. [CrossRef]
17. Shiraishi, K.; Oba, T.; Suzuki, M.; Ishikawa, K. Subsilic magnesian potassium-hastingsite from the Prince Olav Coast, East Antarctica. *Mineral. Mag.* **1994**, *58*, 621–627. [CrossRef]
18. Korinevsky, V.G.; Korinevsky, E.V. Potassic-magnesiohastingsite (K,Na)Ca_2(Mg,Fe^{2+})$_4$(Fe^{3+},Al,Ti)[$Si_6Al_2O_{22}$](OH,Cl)$_2$—The new mineral species of amphiboles. *Zap. RMO* **2006**, *2*, 49–57. (In Russian)
19. Bojar, H.-P.; Walter, F. Fluoro-magnesiohastingsite from Dealul Uroi (Hunedoara county, Romania): Mineral data and crystal structure of a new amphibole end-member. *Eur. J. Mineral.* **2006**, *18*, 503–508. [CrossRef]
20. Aksenov, S.; Chukanov, N.V. The crystal structure of a fluorine-dominant titanium calcium amphibole from the Eifel paleovolcanic area, Germany. *Z. Kristallogr.* **2016**, *231*, 385–390. [CrossRef]
21. Zaitsev, A.N.; Avdontseva, E.Y.; Britvin, S.N.; Demény, A.; Homonnay, Z.; Jeffries, T.E.; Keller, J.; Krivovichev, V.G.; Markl, G.; Platonova, N.V.; et al. Oxo-magnesio-hastingsite, $NaCa_2(Mg_2Fe^{3+}{}_3)(Al_2Si_6)O_{22}O_2$, a new anhydrous amphibole from the Deeti volcanic cone, Gewgory rift, northern Tanzania. *Mineral. Mag.* **2013**, *77*, 2773–2792. [CrossRef]
22. Oberti, R.; Zema, M.; Boiocchi, M.; Tarantino, S.; Welch, M.D. HT-induced processes in monoclinic and orthorhombic amphiboles and their effects on thermodynamic models. *Geophys. Res. Abstr. EGU2011* **2011**, *13*, 11183.
23. Tribaudino, M.; Hovis, G.L.; Almer, C.; Leaman, A. Thermal expansion of minerals in the amphibole supergroup. *Am. Mineral.* **2022**, in press. [CrossRef]
24. Drugov, G.M.; Sizykh, A.I.; Bulanov, V.A. Geological models of mica-bearing junction of the Slyudanskaya and Sogdioddonskaya groups of deposits in the Mamsk province. *Bull. Irkutsk State Univ. Ser. Earth Sci.* **2015**, *13*, 58–77.
25. Whitney, D.L.; Evans, B.W. Abbreviations for names of rock-forming minerals. *Am. Mineral.* **2010**, *95*, 185–187. [CrossRef]
26. Verkaeren, J. Les grenats biréfringents des skarns à magnétite de San Leone (Sardaigne SW). *Bull. Soc. Franc. Mineral. Cristallogr.* **1971**, *94*, 492–499. (In French) [CrossRef]
27. Lessing, P.; Standish, R.P. Zoned garnet from Crested Butte, Colorado. *Am. Mineral.* **1973**, *58*, 840–842.
28. Takeuchi, Y.; Haga, N. Optical anomaly and structure of silicate garnets. *Proc. Jpn. Acad.* **1976**, *52*, 228–231. [CrossRef]
29. Yang, S.-Y.; Zhang, R.-X.; Jiang, S.-Y.; Xie, J. Electron probe microanalysis of variable oxidation state oxides: Protocol and pitfalls. *Geostand. Geoanal. Res.* **2018**, *42*, 131–137. [CrossRef]
30. Finkelshtein, A.L.; Chubarov, V.M. X-ray fluorescence determination of $FeO/Fe_2O_3{}^{tot}$ ratio in igneous rocks. *X-ray Spectrom.* **2010**, *39*, 17–21. [CrossRef]
31. Chubarov, V.M.; Finkelshtein, A.L. Determination of divalent iron content in igneous rocks of ultrabasic, basic and intermediate compositions by a wavelength-dispersive X-ray fluorescence spectrometric method. *Spectrochim. Acta B* **2015**, *107*, 110–114. [CrossRef]
32. Chubarov, V.M.; Amosova, A.A.; Finkelshtein, A.L. Determination of iron and sulfur valence state in coal ashes by wavelength-dispersive X-ray fluorescence spectrometric technique. *Spectrochim. Acta B* **2020**, *163*, 105745. [CrossRef]
33. Chubarov, V.M.; Finkelshtein, A.L.; Suvorova, L.F.; Kostrovitsky, S.I. Determination of iron valence state in picroilmenites by electron probe microanalysis and x-ray fluorescence analysis. *Zap. RMO* **2012**, *141*, 83–91. (In Russian)
34. Bruker APEX2. *Version 2014.11-0*; Bruker AXS Inc.: Madison, WI, USA, 2014.
35. CrysAlis, PRO. *Version 1.171.35.21*; Agilent Technologies Ltd.: Yarnton, UK, 2018.
36. Betteridge, P.W.; Carruthers, J.R.; Cooper, R.I.; Prout, K.; Watkin, D.J. Crystals version 12: Software for guided crystal structure analysis. *J. App. Cryst.* **2003**, *36*, 1487. [CrossRef]
37. Oberti, R.; Hawthorne, F.C.; Cannillo, E.; Cámara, F. long-range order in amphiboles. *Rev. Mineral. Geochem.* **2007**, *67*, 125–171. [CrossRef]
38. Hawthorne, F.; Oberti, R. Amphiboles: Crystal structure. *Rev. Mineral. Geochem.* **2007**, *67*, 1–54. [CrossRef]
39. Momma, K.; Izumi, F. VESTA 3 for three-dimensional visualization of crystal, volumetric and morphology data. *J. Appl. Cryst.* **2011**, *44*, 1272–1276. [CrossRef]
40. Bruker: Topas V4. *General Profile and Structure Analysis Software For Powder Diffraction Data*; Bruker AXS Inc.: Karlsruhe, Germany, 2008.
41. Langreiter, T.; Kahlenberg, V. TEV—A program for the determination of the thermal expansion tensor from diffraction data. *Crystals* **2015**, *5*, 143–153. [CrossRef]
42. Locock, A.J. An Exel spreadsheet to classify chemical analyses of amphiboles following the IMA 2012 recommendations. *Comput. Geosci.* **2014**, *62*, 1–11. [CrossRef]
43. Robinson, K.; Gibbs, G.V.; Ribbe, P.H. Quadratic elongation: A quantitative measure of distortion in coordination polyhedra. *Science* **1971**, *172*, 567–570. [CrossRef]

44. Renner, B.; Lehmann, G. Correlation of angular and bond length distortions in TO_4 units in crystals. *Z. Kristallogr.* **1986**, *175*, 43–59. [CrossRef]
45. Gagnè, O.C.; Hawthorne, F.C. Comprehensive derivation of bond-valence parameters for ion pairs involving oxygen. *Acta Cryst.* **2015**, *B71*, 562–578. [CrossRef] [PubMed]
46. Breese, N.E.; O'Keeffe, M. Bond-valence parameters for solid. *Acta Cryst.* **1991**, *B47*, 192–197. [CrossRef]
47. Oberti, R.; Ungaretti, L.; Cannillo, E.; Hawthorne, F. The mechanism of Cl incorporation in amphibole. *Am. Mineral.* **1993**, *78*, 746–752.
48. Oberti, R.; Ungaretti, L.; Cannillo, E.; Hawthorne, F.; Memmi, I. Temperature-dependent Al order-disorder in the tetrahedral double chain of *C*2/*m* amphiboles. *Eur. J. Mineral.* **1995**, *7*, 1049–1063. [CrossRef]
49. Oberti, R.; Boiocchi, M.; Zema, M. Thermoelasticity, cation exchange, and deprotonation in Fe-rich holmquistite: Toward a crystal-chemical model for the high-temperature behavior of orthorhombic amphiboles. *Am. Mineral.* **2019**, *104*, 1829–1839. [CrossRef]
50. Oberti, R.; Boiocchi, M.; Zema, M.; Hawthorne, F.; Redhammer, G.; Susta, U.; Della Ventura, G. The high-temperature behavior of riebeckite: Expansivity, deprotonation, selective Fe oxidation and a novel cation disordering scheme for amphiboles. *Eur. J. Mineral.* **2018**, *30*, 437–449. [CrossRef]
51. Della Ventura, G.; Mihailova, B.; Susta, U.; Castelli Guidi, M.; Marcelli, A.; Schlüter, J.; Oberti, R. The dynamics of Fe oxidation in riebeckite: A model for amphiboles. *Am. Mineral.* **2018**, *103*, 1103–1111. [CrossRef]
52. Oberti, R.; Boiocchi, M.; Zema, M.; Della Ventura, G. Synthetic potassic-ferro-richterite: 1. Composition, crystal structure refinement, and HT behavior by in operando single-crystal X-ray diffraction. *Can. Mineral.* **2016**, *54*, 353–369. [CrossRef]
53. Della Ventura, G.; Susta, U.; Bellatreccia, F.; Marcelli, A.; Redhammer, G.; Oberti, R. Deprotonation of Fe-domonant amphiboles: Single-crystal HT-FTIR spectroscopic studies of synthetic potassic-ferro-richterite. *Am. Mineral.* **2017**, *102*, 117–125. [CrossRef]
54. Iezzi, G.; Della Ventura, G.; Hawthorne, F.C.; Pedrazzi, G.; Robert, J.L.; Novembre, D. The (Mg,Fe^{2+}) substitution in ferri-clinoholmquistite, $\square Li_2(Mg,Fe^{2+})_3Fe^{3+}{}_2O_{22}(OH)_2$. *Eur. J. Mineral.* **2005**, *17*, 733–740. [CrossRef]
55. Ishida, K. Assignment of infrared OH-stretching bands in calcic amphiboles through deuteration and heat treatment. *Am. Mineral.* **2006**, *91*, 871–879. [CrossRef]
56. Burns, R.G.; Strens, R.G.J. Infrared study of the hydroxyl bonds in clinoamphiboles. *Science* **1966**, *153*, 890–892. [CrossRef]
57. Della Ventura, G. Recent developments in the synthesis and characterization of amphiboles. Synthesis and crystal chemistry of richterite. *Trends Mineral.* **1992**, *1*, 153–192.
58. Ishida, K. Identification of infrared OH librational bands of talc-willemseite solid solutions and Al (IV)-free amphiboles through deuteration. *Mineral. J.* **1990**, *15*, 93–104. [CrossRef]
59. Sergeeva, A.V.; Zhitova, E.S.; Nuzhdaev, A.A.; Zolotarev, A.A.; Bocharov, V.N.; Ismagilova, R.M. Infrared and Raman spectroscopy of ammoniovoltaite, $(NH_4)_2Fe^{2+}{}_5Fe^{3+}{}_3Al(SO_4)_{12}(H_2O)_{18}$. *Minerals* **2020**, *10*, 781. [CrossRef]
60. Bogdanov, A.; Kaneva, E.; Shendrik, R. New insights into the crystal chemistry of elpidite, $Na_2Zr[Si_6O_{15}]\cdot 3H_2O$ and $(Na_{1+y}Ca_x\square_{1-x-y})_{\Sigma=2}Zr[Si_6O_{15}]\cdot(3-x)H_2O$, and ab initio modeling of IR spectra. *Materials* **2021**, *14*, 2160. [CrossRef] [PubMed]
61. Omori, K. Analysis of the infrared absorption spectrum of diopside. *Am. Mineral.* **1971**, *56*, 1607–1616.
62. Burns, R.G. *Mineralogical Application of Crystal Field Theory*; Cambridge University Press: Cambridge, UK, 1993. [CrossRef]
63. Goldman, D.S.; Rossman, G.R.; Dollase, W.A. Channel constituents in cordierite. *Am. Mineral.* **1977**, *62*, 1144–1157.
64. Taran, M.N.; Langer, K. Electronic absorption spectra of Fe^{2+} ions in oxygen-based rock-forming minerals at temperatures between 297 and 600 K. *Phys. Chem. Miner.* **2001**, *28*, 199–210. [CrossRef]
65. Fontana, I.; Lauria, A.; Spinolo, G. Optical absorption spectra of Fe^{2+} and Fe^{3+} in aqueous solutions and hydrated crystals. *Phys. Status Solidi B* **2007**, *244*, 4669–4677. [CrossRef]
66. Abragam, A.; Bleaney, B. *Electron Paramagnetic Resonance of Transition Ions*; Oxford University Press: Oxford, UK, 2012.
67. Shongwe, M.S.; Al-Rahbi, S.H.; Al-Azani, M.A.; Al-Muharbi, A.A.; Al-Mjeni, F.; Matoga, D.; Gismelseed, A.; Al-Omari, I.; Yousif, A.; Adams, H.; et al. Coordination versatility of tridentate pyridyl aroylhydrazones towards iron: Tracking down the elusive aroylhydrazono-based ferric spin-crossover molecular materials. *Dalton Trans.* **2012**, *41*, 2500. [CrossRef] [PubMed]
68. Skogby, H.; Rossman, G.R. OH^- in pyroxene; an experimental study of incorporation mechanisms and stability. *Am. Mineral.* **1989**, *74*, 1059–1069.
69. Burt, D.M. Metasomatic zoning in Ca-Fe-Si exoskarns. In *Geochemical Transport And Kinetics*; Hofmann, A.W., Giletti, H.S., Yoder, H.S., Jr., Yund, R.A., Eds.; Carnegie Institution of Washington: Washington, DC, USA, 1974; Volume 634, pp. 287–293.
70. Pertsev, N.N. Skarns as magmatic and as postmagmatic formations. *Int. Geol. Rev.* **1974**, *16*, 572–582. [CrossRef]
71. Burt, D.M. Mineralogy and petrology of skarn deposits. *Soc. Ital. Mineral. Petrol. Rend.* **1977**, *33*, 859–873.
72. Meinert, L.D.; Dipple, G.M.; Nicolescu, S. World skarn deposits. *Econ. Geol.* **2005**, *100*, 299–336. [CrossRef]
73. Einaudi, M.T.; Burt, D.M. Introduction; terminology, classification, and composition of skarn deposits. *Econ. Geol.* **1982**, *77*, 745–754. [CrossRef]
74. Meinert, L.D. Skarns and Skarn Deposits. *Geosci. Can.* **1992**, *19*, 145–162.
75. Alaminia, Z.; Mehrabi, B.; Razavi, S.M.H.; Tecce, F. Mineral chemistry, petrogenesis and evolution of the Ghorveh-Seranjic skarn, Northern Sanandaj Sirjan Zone, Iran. *Mineral. Petrol.* **2020**, *114*, 15–38. [CrossRef]